Elastic-Stiffness Distribution on Dual-Phase Stainless Steel Studied by Resonance Ultrasound Microscopy

Hirotsugu Ogi, Hiroki Niho, and Masahiko Hirao

Graduate School of Engineering Science, Osaka University
Machikaneyama 1-3, Toyonaka, Osaka 560-8531, Japan

Abstract

Distribution of the elastic-stiffness coefficient on a dual-phase stainless steel is studied by resonance-ultrasound microscopy and electron-backscattering patterns. Using a monocrystal langasite oscillator, the resonance-frequency change due to the contact with the material is measured contactlessly by a solenoid-coil antenna. The theoretical calculation based on the contact between two anisotropic bodies is proposed to determine the contact stiffness from the resonance frequency. The measured stiffness distribution is compared with that predicted from the orientation distribution determined by the electron-backscattering-pattern method. They principally agreed but the stiffness by resonance-ultrasound microscopy is nonuniform even in a single γ-phase grain. The nonuniformity of the chromium concentration can be a principal cause of the stiffness distribution.

Key words: acoustic methods, Resonance Ultrasound Microscopy, Mechanical Properties-elastic behaviour, Steels-dual phases, electron backscattering patterns (EBSP)

Preprint submitted to Elsevier Science Received xx September; accepted xxxxxxx

1 INTRODUCTION

Elastic stiffness of materials provides important knowledge of atomic-bond configurations and thermodynamic features (1; 2). Macroscopically, elastic stiffness reflects microscopic defects through elastic softening and elastic anisotropy (3; 4). Defects such as dislocations and microcracks cause additional strain beyond the perfect-lattice strain, and their nonrandom alignment causes elastic anisotropy. Conventional methods for measuring material's stiffness evaluate macroscopic or averaged moduli. However, studies on elastic stiffness in local regions become more significant because most materials show inhomogeneous microstructures due to nonuniform concentrations of impurity elements, residual-stain distribution, piling-up dislocations, lattice distortion near grain boundaries, and so on.

Atomic-force-acoustic microscopy (AFAM) (5; 6; 7) made it possible to estimate local elastic properties of solids from the resonance frequency of a cantilever contacting the material with a needle-tip's free end. It estimates the elastic stiffness in a nanometer resolution, but an absolute determination of material's stiffness has been difficult because the vibrating cantilever is fixed to the grip and the piezoelectric oscillator is attached on it. To calculate the resonance frequencies of such a composite-resonator system, exact values of dimensions, elastic constants, and mass densities of all participating components must be known. Most significantly, the rigidity and friction at the fixed end of the cantilever affects the resonance frequency because the maximum bending stresses appear on the surface there. Thus, the quantitative determination of the local stiffness definitely requires an isolated oscillator in the resonator system.

We recently demonstrated a novel microscopic method of measuring local stiffness of solids, which we call resonance-ultrasound microscopy (RUM) (8; 9; 10). Mechanical resonance frequencies of an oscillator change when it is in contact with a material, depending on the elastic stiffness of the material at the contact area. The material's local stiffness can be inversely determined from the measured oscillator's resonance frequencies. However, the determination of the local stiffness prohibits any contacts on the oscillator surfaces, even for holding, except for the contact with the measuring material. Neither wires nor electrodes are allowable. We fulfilled this critical demand using a monocrystal langasite ($La_3Ga_5SiO_{14}$) oscillator; the high piezoelectricity of langasite allows us to measure its resonance frequencies with the electric fields in a noncontacting manner. Low temperature derivatives of the elastic constants of langasite allow us to perform the measurement without controlling temperature.

Here, we further improve our RUM by making the oscillator isolated completely, leading to enhanced sensitivity. We also formulate the resonance-

frequency change caused by the contact with anisotropic materials. The Hertzian contact theory between two anisotropic bodies is applied to calculate the effective stiffness contributing to the resonator system.

There are three purposes in the present study. First, we demonstrate the usefulness, correctness, and high sensitivity of our stiffness microscopy for studies of elastic properties of small-scale materials. Second, we show the necessity of considering anisotropy of the specimen for evaluating the contact stiffness, and then we clarify the validity of the obtained formula. Third, we study the nonuniformity of elastic stiffness in a single crystallite. For these proposes, we use a dual-phase stainless steel and compare the stiffness measured by RUM with that predicted from crystallographic orientations measured by the electron-backscattering patterns (EBSP).

2 MATERIAL

Examined specimen was the dual-phase stainless steel (JIS-SCS14A). It consists of ferritic-phase (α-phase) matrix and austenitic-phase (γ-phase) island precipitates (see Fig. 3(a)). The chemical composition is given in Table 1. The volume fraction of the γ phase was determined to be 74.2% by observing the surface microstructure by scanning-electron microscopy. The EPMA measurement was carried out to estimate the chromium concentrations in the α and γ phases as shown in Table 1.

This dual-phase microstructure provides high corrosion resistance, high toughness and high strength, and it has been used in nuclear power plants as casings for primary coolant systems(11; 12).

3 MEASUREMENTS

Our previous RUM system (8; 9; 10) entailed contacts between the langasite oscillator and the side faces of the solenoid coil, deteriorating the sensitivity of the frequency to the material's modulus. Here, we develop a completely isolated system as shown in Fig. 1, realizing a *free* oscillation. The rectangular-parallelepiped langasite monocrystal is held by a fixture at the center nodal lines on the side faces. The langasite oscillator measures 7 mm x 2 mm x 2 mm along X, Y, Z directions of trigonal crystallographic axes, respectively. We choose the X direction of the crystal to be vertical because smaller X-axis Young's modulus provides higher sensitivity to the specimen's stiffness. A natural-diamond tip is attached at the center on the bottom surface of the crystal. A solenoid-coil antenna is embedded in the cylindrical guide, which

allows the vertical movement of the oscillator together with the fixture. The specimen is put on an X-Y-Z stage. The system is placed in a vacuum ($\sim$ 1 Pa) to avoid the acoustical coupling with the atmosphere.

A sinusoidal voltage applied to the solenoid-coil antenna causes the quasistatic electric field (nonrotational component) E_x in the vertical direction, which results in the principal stresses $-e_{11}E_x$ in the X direction and $e_{11}E_x$ in the Y direction via the converse piezoelectric effect. e_{11} denotes a piezoelectric coefficient of materials showing 32-point-group symmetry. Thus, this setup causes breathing vibrations (A_g vibration group (13)) of the oscillator. The same antenna receives the vibrational amplitudes through the piezoelectric effect. A frequency scan yields the resonance spectrum, requiring neither wires nor electrodes on the oscillator surfaces.

We utilized the fundamental mode of the breathing vibration (A_g-1) because it has nodal lines at the center on the side faces, at which the oscillator was supported by the fixture, and an antinode point at the center on the bottom surface, where the tip was attached to touch the specimen, thereby achieving a high sensitivity. The setup in Fig. 1 makes the frequency sensitivity to the specimen's modulus higher than that in the previous configuration (8; 9) by a factor larger than 10.

Before the elastic-stiffness mapping, the EBSP measurement was carried out with the instrument INCA Crystal 300 (OXFORD Instruments). The applied accelerating voltage was 30 kV. The surface layer about 30 μm thick was removed chemically to obtain a nonstrained surface. Kikuchi patterns were then obtained with the 7-μm step to determine all three Euler angles, and Miller indices (h, k, l) and (u, v, w).

We measured the resonance frequency with the 5-μm step on the same area examined by EBSP. At each measuring point, the resonance frequency was measured before and after making the contact and the frequency shift caused by the contact was recorded. The biasing force F of 0.019 N was applied from the gravity, which remained unchanged and independent of the surface nonflatness. After each contact measurement, the specimen departed from the tip and moved to the next point. The tip thus did not scratch the specimen surface.

4 VIBRATIONAL ANALYSIS

The contact interface between the tip and specimen is equivalent to an elastic spring of the contact stiffness K (6; 14; 15; 16). The resonance frequency is calculated accurately by Lagrangian minimization with the Rayleigh-Ritz

method (13). The system Lagrangian consists of the elastic strain energy, electromechanical coupling energy, electrostatic energy of the langasite crystal (13; 17); kinetic energy of the tip; and the elastic-spring energy at the tip-specimen interface (10). No frictional effect is involved. The displacements and electric potential are approximated by a combination of many basis functions of Legendre polynomials (Rayleigh-Ritz approach). The calculation of the resonance frequencies requires dimensions, elastic and piezoelectric coefficients of the langasite crystal, mass of the tip, which are measurable, and the contact stiffness K.

Figure 2 shows the calculated dependence of the resonance frequencies of A_g-group modes on the contact stiffness. The fundamental mode (A_g-1) shows the highest sensitivity to the contact stiffness, which is attributed to the minimum number of antinodes, one of which is acting as a probe. With this observation, we determined the contact stiffness at individual points by driving the oscillator in the A_g-1 resonance.

5 CONTACT STIFFNESS

Many studies with AFAM and RUM analyzed local elastic properties of solids using classical Hertzian-contact model (6; 8; 9; 14; 15; 16), which assumes the contact between two isotropic materials. This model yielded the contact stiffness K_{iso} of the form

$$K_{iso} = \sqrt[3]{6FRE^{*2}} \tag{1}$$

Here, R denotes the tip radius and E^* denotes the effective Young's modulus given by

$$E^* = \left[\frac{1-\nu_t^2}{E_t} + \frac{1-\nu_s^2}{E_s}\right]^{-1} \tag{2}$$

ν and E are Poisson's ratio and Young's modulus, and subscripts t and s denote quantities of the tip and the specimen, respectively. This approach has been adopted to evaluate the local Young's modulus of the specimen. However, many materials show elastic anisotropy in local regions and the validity of this model is doubtful.

We analytically formulated the relationship between the contact stiffness and the elastic constants of materials for the case that two orthorhombic bodies are in contact with each other, keeping their orthogonal axes parallel to the

contact surface (18), following Willis (19) and Swanson (20). The result gave the contact stiffness for anisotropic materials K_{aniso} as

$$K_{aniso} = \sqrt[3]{\frac{48FRI_1}{I_0^3}} \tag{3}$$

Here, I_0 and I_1 are given by integrating the Green function $\hat{G}$ for the point-force indentation, including the orthorhombic elastic-stiffness tensors of the tip and specimen (19):

$$I_0 = \sum_{i=t,s} \int_0^{2\pi} \hat{G}_i(\epsilon\eta_y, \eta_z) d\theta, I_1 = \sum_{i=t,s} \int_0^{2\pi} \hat{G}_i(\epsilon\eta_y, \eta_z) \eta_y^2 d\theta$$

$\eta_y = \cos\theta$ and $\eta_z = \sin\theta$; θ denotes the angle of the polar-coordinate system on the contact-interface plane. ϵ is the ratio between the major and minor axes of the ellipsoid of the contact interface and it is obtained by an iterative calculation (20), although it is close to unity.

Crystallite orientations normal to the surface are usually off-principal directions and the above results cannot be used generally. In this study, we average the elastic-stiffness tensor over the polar angle about the normal direction to the surface using the Hill averaging method: The averaged elastic stiffness tensor $< C_{ijkl} >$ is given by

$$< C_{ijkl} >= \frac{1}{2} \left[\frac{1}{2\pi} \int_0^{2\pi} C_{ijkl}(\theta) d\theta + \left(\frac{1}{2\pi} \int_0^{2\pi} s_{ijkl}(\theta) d\theta \right)^{-1} \right] \tag{4}$$

where s_{ijkl} denotes the elastic-compliance tensor. Thus, this averaging procedure yields transversely isotropic (or hexagonal symmetry) stiffness tensors at the measuring points, which accept the formula derived for orthorhombic materials (Eq.(3)).

By comparing measured and predicted stiffnesses, we discuss the effect of material's elastic anisotropy on the contact stiffness.

6 RESULTS

Figure 3 compares the microstructure observed by scanning-electron microscopy, the orientation direction normal to the surface calculated from the EBSP results, and the frequency increase measured by RUM. Our microscopy clearly

shows the difference of the elastic stiffness of the two phases; higher stiffness of γ-phase grains than that of α-phase grains. It also demonstrates the stiffness difference among crystallites with different orientations. $<111>$-oriented γ-phase grains show larger modulus, which is reasonable because (111) planes are closest-packing planes in f.c.c. crystals.

Figure 4 compares images of the contact stiffness determined from the frequency shift in Fig. 3(c) and that calculated by Eq.(3), showing good agreement. Figure 5 focuses on distribution of the stiffness in γ-phase crystallites. The RUM measurement yields higher stiffness in the center region of each crystallite, while EBSP predicts the uniform stiffness in a single crystallite.

Figure 6 compares the calculated and measured contact stiffness for γ-phase grains in Fig. 3. (From the EBSP measurements, we identified 60 grains of γ phase in Fig. 3(a).) Clearly, the anisotropic-contact model shows much better agreement with the measurement.

7 DISCUSSIONS

In this paper, we focus on elastic properties of γ-phase grains. The cubic elastic constants of pure f.c.c. iron are reported (21) as shown in Table 2. However, there is no report on monocrystal elastic constants of the Fe-Cr alloy and we had to estimate them to calculate the contact stiffness in γ-phase grains. The elastic constants will be smaller than the pure-f.c.c.-iron values because the substitutional chromium causes lattice distortion as analyzed by Zener (22). The anisotropy factor $A = 2C_{44}/(C_{11} - C_{12})$ will be hardly affected though. Our EPMA measurement shows that the chromium concentration in γ-phase grains is close to that in a standard SUS304 steel (chromium concentration is between 18-20 mass%), whose elastic constants are reported (23) and given in Table 2. Considering that an isotropic aggregate of the γ-phase monocrystal should yield the elastic constants of the polycrystalline SUS304 steel, we inversely determined the three monocrystal elastic constants of the γ phase alloy. Assumptions made were (i) the anisotropic factor A is the same as that of the pure-f.c.c. iron and (ii) the Hill averaging of the monocrystal elastic constants provides the reported values for polycrystalline SUS304 steel. The results are shown in Table 2.

From the EBSP measurement, we calculated the elastic-stiffness tensor at individual measuring points. The contact stiffness was then obtained either by Eq. (1) or Eq. (3). Such a calculation requires the tip radius, which is, however, ambiguous because of the non-perfect sphere shape of the conical diamond tip. We therefore fitted the tip radius to obtain the same average contact stiffness by calculations as that by the measurement, resulting in R=9.02 μm.

We used the normal Young's modulus to the surface as the material's modulus E_s in Eq.(2). The stiffness K_{iso} in Fig.6 is thus calculated using the normal Young's modulus of γ-phase grains. The contact stiffness from this isotropic contact model is however much more sensitive to the grain orientation than the measured stiffness and it cannot explain the measurement quantitatively. On the other hand, the contact stiffness calculated by the anisotropic-contact model K_{aniso} quantitatively agrees with the measured stiffness: Indeed, images of the contact stiffness measured by RUM and that calculated by Eq.(3) are nearly identical as demonstrated in Fig. 4, indicating validity and importance of considering the material's anisotropy for evaluating the elastic properties in a point-contact measurement including RUM, AFAM, and all indentation measurements.

We note that the stiffness is nonuniform even in a single grain as seen in Fig. 5: The stiffness predicted from the EBSP results is almost uniform in a single crystallite, but the stiffness determined by RUM is larger inside grains than near grain boundaries. We attribute this to the nonuniform chromium concentration: The chromium concentration is higher in α phase than in γ phase and it can increase in γ grains near the α-γ boundaries due to diffusion. Zener (22) indicated that Young's moduli of binary alloys decreased as the concentrations of the substitutional impurity atoms increased. Therefore, the stiffness decrease near the γ-phase grain boundaries indicates the larger concentration of chromium there.

Another possibility is the influence of the softer α phase. The radius of the contact area is estimated to be 1-2 μm and the measured stiffness may reflect the softer α phase in regions very close to the grain boundaries. However, the stiffness change in a crystallite occurs in a larger special scale than the contact area and this will be not the principal cause.

8 CONCLUSIONS

A completely isolated resonator system was developed for quantitatively evaluating local elastic stiffness of solids. The vibration of the langasite oscillator was excited and detected by the solenoid-coil antenna in the noncontacting manner to isolate the oscillator from all other effective contacts than the specimen. This home-built microscopy demonstrated high potential in the study of material's local elastic properties.

The EBSP measurement was done to predict the local elastic constants from the crystallite orientation. Comparison of the stiffnesses determined by the RUM and EBSP strongly showed that the contact stiffness must be calculated considering elastic anisotropy of the contacting bodies. The elastic stiffness

appeared nonuniform even in a single grain of the γ phase in the dual-phase stainless steel. This stiffness distribution was interpreted as the nonuniform chromium concentration due to diffusion from the high-chromium concentration area in the α phase.

ACKNOWLEDGEMENT

This study was supported by Industrial Technology Research Grant Program in 2004 from the New Energy and Industrial Technology Development Organization (NEDO).

References

[1] Anderson O. Equations of State of Solids for Geophysics and Ceramic Science. New York: Oxford Univ. Press; 1995.

[2] Keppens V, Migliori A. Elastic Properties and Thermodynamics. In Handbook of Elastic Properties of Solids, Liquids and Gases. eds Levy M, Bass H, Stern, R. San Diego;Academic 2001:173.

[3] Ogi H, Shimoike G, Hirao M, Takashima K, Higo Y. J Appl Phys 2002;91:4857.

[4] Nakamura N, Ogi H, Hirao M. Acta Mater 2004;52:765.

[5] Yamanaka K, Ogiso H, Kolosov O. Appl Phys Lett 1994;64:178.

[6] Rabe U, Turner J, Arnold W. Appl Phys A 1998;66:S277.

[7] Yamanaka K, Tsuji T, Noguchi A, Koike T, Mihara T. Rev Sci Inst 2000;71:2403.

[8] Ogi H, Tian J, Tada T, Hirao M. Appl Phys Lett 2003;83:464.

[9] Tian J, Ogi H, Tada T, Hirao M. J Appl Phys 2003;94:6472.

[10] Ogi H, Tada T, Tian J, Hirao M. Jpn J Appl Phys 2005;44:4381.

[11] Ogi H, Hirao M. Res Nondestr Eval 1997;9:171.

[12] Tane M, Ichitsubo T, Ogi H, Hirao M Scripta Mater 2003;48:229.

[13] Ohno I. Phys Chem Minerals 1990;17:371.

[14] Yamanaka K, Nakano S, Appl Phys A 1998;66:S313.

[15] Yaralioglu GG, Degertekin FL, Crozier KB, Quate CF. J Appl Phys 2000;87:7491.

[16] Tian J, Ogi H, Hirao M. J Appl Phys 2004;95:8366.

[17] Ogi H, Nakamura N, Sato K, Hirao M, Uda S. IEEE Trans Ultrason Ferroelectr Freq Ctrl 2003;50:553.

[18] Tian J, Ogi H, Hirao M. Appl Phys Lett 2005;87:204107.

[19] Willis JR. J Mech Phys Solids 1966;14:163.

[20] Swanson SR. Int J Solids Struct 2004;41:1945.

[21] Ledbetter H, Kim S. Monocrystal Elastic Constants and Derived Properties of The Cubic and The Hexagonal Elements: in Handbook of Elastic Properties of Solids, Liquids, and Gases, Vol. 2. San Diego:Academic 2001.

[22] Zener C. Acta Cryst 1949;2:163.

[23] Ledbetter H, J Appl Phys 1981;52:1587.

Table 1
Chemical contents (mass %) except Fe of the dual-phase stainless steel (JIS-SCS14A).

Cr	C	Si	Mn	P	S	Ni	Mo
20.65 (α:18.4, γ:27.5)	0.052	1.35	0.70	0.028	0.004	9.16	2.48

Table 2
Elastic constants (GPa) of pure-f.c.c. iron (21), polycrystalline SUS304 steel (23), and monocrystal Fe-Cr alloy inversely determined here. A denotes the anisotropy factor, and B and G denote the bulk modulus and shear modulus of aggregates, respectively.

	C_{11}	C_{12}	A	C_{44}	B	G
f.c.c. Fe	276	173.5	2.67	136.3	207.7	92.1
SUS304	-	-	-	-	158	77.4
Fe-18.4-mass%Cr (present)	215.1	129.0	2.67	114.6	158	77.4

Figure Caption

Fig. 1 Setup of the RUM oscillator. Monocrystal langasite oscillator is held by a fixture at the nodal lines on the side surfaces. The weights of the oscillator and fixture cause the biasing force for the contact with the specimen. The solenoid-coil antenna makes a noncontacting measurement of the oscillator's resonance frequency.

Fig. 2 Sensitivity of the resonance frequencies of A_g-vibration modes to the contact stiffness calculated by Lagrangian minimization with the Rayleigh-Ritz method.

Fig. 3 (a) Image obtained by scanning-electron microscopy of the dual-phase stainless steel (JIS-SCS14A), (b) image of the crystallographic orientation normal to the surface of the γ phase determined by the EBSP measurement, and (c) image of the resonance frequency measured by RUM.

Fig. 4 Image of the contact stiffness determined from the measured resonance frequency (left) and that calculated by the anisotropic-contact model (Eq.(3)) using Euler angles obtained by the EBSP measurement.

Fig. 5 Contact-stiffness distribution in γ-phase grains measured by RUM (left) and that predicted by the anisotropic-contact model with the EBSP results.

Fig. 6 Comparison between the contact stiffness measured by RUM K_{meas} and the contact stiffnesses K_{calc} calculated using the isotropic and anisotropic models. The slope of the solid line is one.

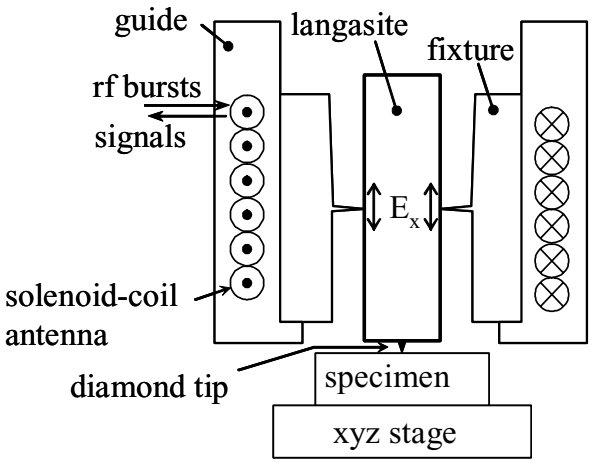
guide
langasite
fixture
rf bursts
signals
E_x
solenoid-coil
antenna
diamond tip
specimen
xyz stage

Fig. 1.

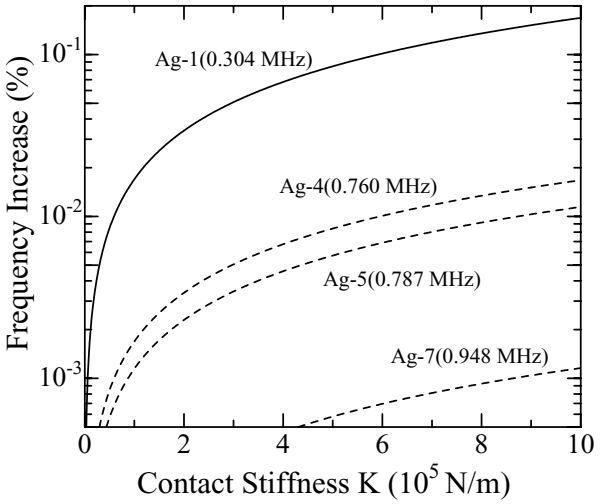
Frequency Increase (%)
10^{-1}
10^{-2}
10^{-3}
Ag-1(0.304 MHz)
Ag-4(0.760 MHz)
Ag-5(0.787 MHz)
Ag-7(0.948 MHz)
0
2
4
6
8
10
Contact Stiffness K (10^5 N/m)

Fig. 2.

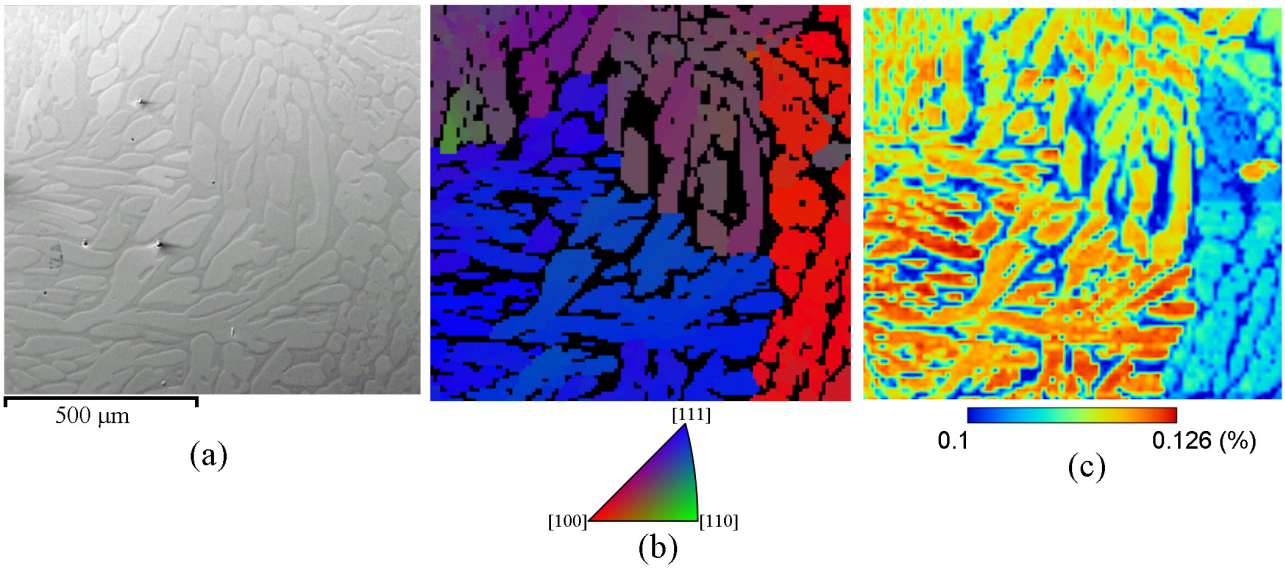

Fig. 3.

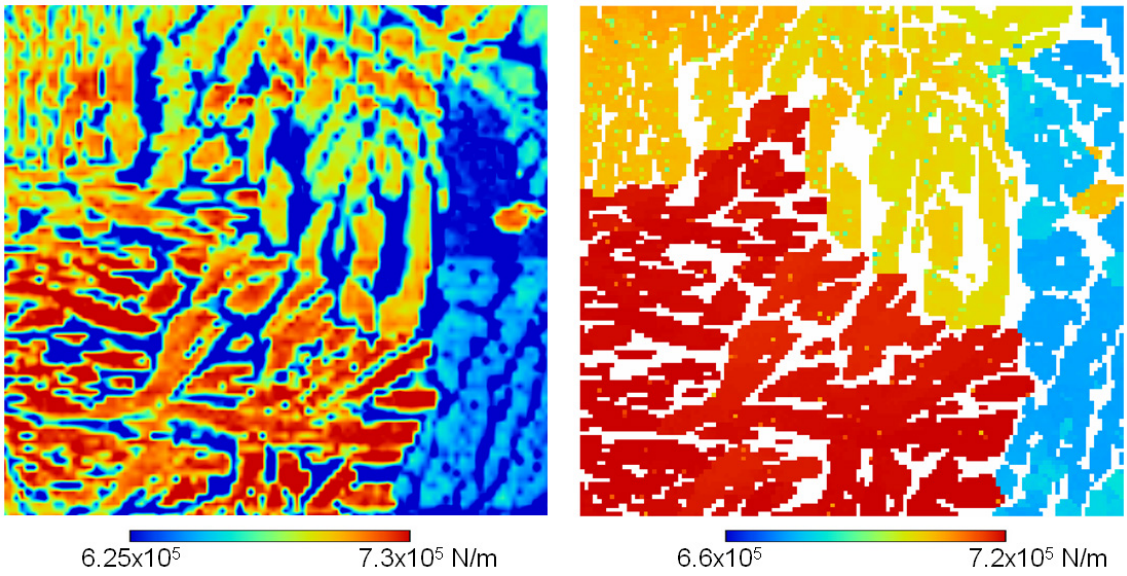

Fig. 4.

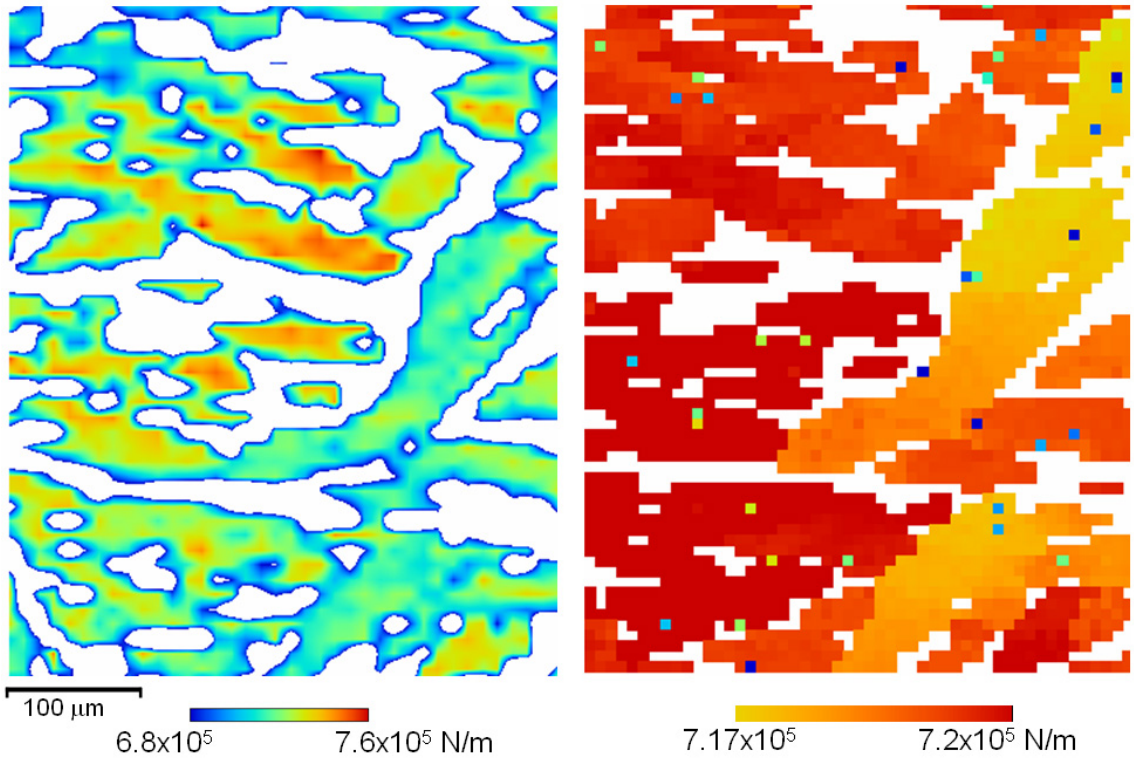

Fig. 5.

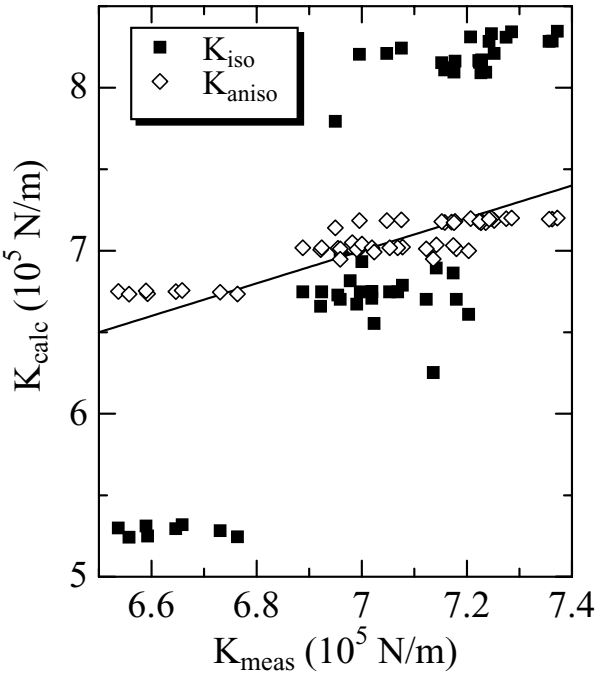

Fig. 6.